RSC Advances

PAPER

View Article Online
View Journal | View Issue

Cite this: *RSC Adv.*, 2026, **16**, 11972

Bio-carbon quantum dot modified TiO_2 nanocrystals for photocatalytic degradation of PLA and PET microplastics

Min Zheng, *[a] Yangyi Wang,[b] Yiheng Liu,[a] Xiaoyan Jiang,[a] Yannan Zhang[a] and Jinghao Huo [c]

Microplastic pollution is widespread, infiltrating water bodies and soil, entering the food chain, and thereby posing threats to ecosystems and human health. In this study, anatase titanium dioxide (TiO_2) was prepared *via* a hydrothermal method and subsequently modified with bio-based carbon quantum dots (CQDs). The composite exhibited optimal performance when the concentration of the carbon source (citric acid) was 0.17 M, yielding carbon dots with an observable size of approximately 4.18 nm. The formation of Ti–O–C chemical bonds between the carbon dots and TiO_2 was observed. Compared to pristine TiO_2, the CQDs@TiO_2 composite displayed a reduced bandgap, significantly enhanced light absorption in the visible region, improved photogenerated charge carrier transport, and suppressed non-radiative recombination, leading to a substantial enhancement in photocatalytic performance. The CQDs@TiO_2 photocatalyst was employed for the photodegradation of polyethylene terephthalate (PET) and polylactic acid (PLA) microplastics under visible light irradiation. The results indicated that under illumination at 100 mW cm^{-2} in a pH 8 buffer solution, CQDs@TiO_2 effectively catalyzed the degradation of alkali-pretreated PET and PLA microplastic samples, with 48 h degradation rates of 28.9% and 59.8%, respectively. The degradation of both types of plastics primarily relied on the synergistic action of $^1O_2$, h^+, $\cdot O_2^-$ and $\cdot OH$ generated by the photocatalyst, both undergoing a degradation process centered on the cleavage of ester bonds. This study not only demonstrates the superior photocatalytic efficacy of the CQDs@TiO_2 composite but also establishes it as a viable strategy for mitigating the urgent challenge of microplastic pollution under near-natural conditions.

Received 5th January 2026
Accepted 19th February 2026

DOI: 10.1039/d6ra00096g

rsc.li/rsc-advances

1. Introduction

With the widespread production and use of plastic products worldwide, plastic pollution has become one of the most pressing environmental issues of our time.[1,2] Among these, microplastics (MPs)—plastic particles, fibers or fragments smaller than 5 millimeters—pose the most challenging problem. Studies have shown that microplastics are widely distributed and can easily accumulate in water, soil and even within living organisms, where they are ingested and transferred along the food chain.[3] Beyond their intrinsic risks, microplastics serve as carriers for diverse organic pollutants. The resulting composite contaminants give rise to expanded ecological and health implications.[4]

Effective removal of microplastics before they enter the water represents the most direct approach to addressing microplastic pollution. Currently, research on microplastic treatment methods remains at the preliminary laboratory exploration stage. According to previous studies, ultraviolet irradiation can induce polymer aging and promote photo-oxidation reactions, leading to their mineralization into carbon dioxide and water.[5] Tian *et al.* were the first to conduct quantitative research on the specific photodegradation of nanoplastics, using ^{14}C radioisotope tracing technology to quantitatively investigate the degradation of polystyrene microplastics suspended in water under UV irradiation. After 48 hours of exposure, 18.1% of the total suspended polystyrene nanoparticles underwent photodegradation.[6] In direct photolysis experiments using natural sunlight, polystyrene microplastics were also found to be broken down into intermediate products such as short-chain carboxylic acids and aromatic compounds.[7] Photocatalysts, under light exposure, can generate hydroxyl radicals, reactive oxygen species, hydrogen peroxide, *etc.*, which actively accelerate the degradation reaction of microplastics, yielding products including carbon dioxide, ketones, alcohols, carboxylic acids and aldehydes.[8,9] Therefore, photocatalysis is considered

[a]*School of Photoelectric Engineering, Changzhou Institute of Technology, Changzhou, Jiangsu 213002, China. E-mail: zhengmin@czust.edu.cn; Tel: +86 18136728660*
[b]*Changzhou Isovolta Technical Composite Co., Ltd, Changzhou, Jiangsu 213002, China*
[c]*School of Materials Science and Engineering, Shaanxi Laboratory of Advanced Materials, Shaanxi University of Science and Technology, Xi'an 710021, China*

a clean technology capable of overcoming microplastic pollution.

TiO_2 is one of the most extensively studied photocatalytic materials and is widely used due to its excellent photocatalytic performance, high stability, non-toxicity and low cost.[10–12] Relevant studies have shown that TiO_2-based photocatalysts can promote the photodegradation of common plastics such as PE, PET, PS, PP, polyvinyl alcohol and PLA.[13–16] Aragón *et al.* reported a detailed experimental analysis of the photocatalytic degradation of PE, with commercial TiO_2 P25 as a catalyst and under the given experimental conditions, after 8 h of treatment, the photocatalytic degradation was evidenced by gravimetric analysis, carbonyl index, particle size reduction and so on.[17] Domínguez-Jaimes *et al.* synthesized three different TiO_2 photocatalysts *via* anodic oxidation and monitored the removal and degradation of PS microplastics under the action of these catalysts. Statistical analysis showed that TiO_2 with a mixed structure (nanotubes/nanograss) was twice as effective in reducing the concentration of PS-NPs in dispersion compared to photolysis using UV light alone.[10] Chattopadhyay *et al.* prepared dynamic "Pac-Man" shaped TiO_2 structures *via* a one-pot method. In a system containing H_2O_2, 28% of polystyrene particles were degraded after 70 h of UV irradiation.[18] He *et al.* utilized zinc oxide tetrapods coated with titanium dioxide to catalytically degrade common PE and PES microplastics under UV irradiation. Complete mass loss for PE and PES was achieved after 480 h and 624 h respectively. Furthermore, the material remained effective in degrading environmental microplastic samples primarily composed of PP, though a longer degradation time (approximately 816 h) was required for the samples to completely lose mass.[19]

Although research on the application of titanium dioxide-based photocatalysts in microplastic degradation has yielded some results, a significant limitation persists due to the relatively wide band gap of TiO_2 (3.0–3.2 eV).[13] Only short-wavelength ultraviolet light (λ < 380 nm) can excite its electrons, yet UV light constitutes only about 3% of the solar spectrum. This severely restricts the practical application of TiO_2 for photocatalytic pollutant degradation under natural sunlight. Therefore, exploring strategies to broaden the light-response range of TiO_2-based photocatalysts and enhance their visible-light absorption is crucial for advancing microplastic degradation in real-world environments.

Among various optimization strategies, surface modification and doping remain the most prevalent.[20,21] Quantum dots (QDs) have emerged as one of the most effective components for constructing composite TiO_2 photocatalysts. This is owing to their advantages, including size-tunable band gaps, high light absorption coefficients, and the ability to form Type-II heterojunctions or Z-scheme charge transfer mechanisms with the host material, thereby facilitating the spatial separation of photogenerated electron–hole pairs. Various QDs, including CdS, CdSe, PbS, carbon quantum dots (CQDs), graphene quantum dots (GQDs), InP, and $CsPbX_3$ perovskite QDs, have been demonstrated to effectively enhance the photocatalytic performance of TiO_2.[22–25] Among them, carbon quantum dots (CQDs) are approximately spherical nanoparticles with a carbon-based framework. They integrate excellent optical properties, ease of functionalization, environmental friendliness, and cost-effectiveness, making them a highly promising class of nanomaterials. Research by scholars such as Qian Wang *al.*[26] and Shiwei Xu[27] has shown that modifying TiO_2 with carbon dots can adjust its band gap, broaden its light-harvesting range, improve electron acceptance and transfer capabilities, and effectively suppress the recombination of photogenerated charge carriers. Furthermore, carbon dots possess surfaces densely functionalized with groups such as hydroxyl, carboxyl, and amino moieties.[28] Different functional groups impart varying chemical structures and surface properties to carbon dots, enabling physical or chemical interactions (*e.g.*, electrostatic interactions, hydrogen bonding, and chelation) with target substances. This can alter their optical response, fluorescence properties, and electron transfer performance.[29,30] In photocatalytic reactions, these surface groups can also influence the adsorption and activation processes of substrates on the catalyst surface.[31] Notably, carbon dots have garnered considerable attention in the field of microplastic remediation. Through optimized synthesis and modification routes, researchers can tailor the particle size, composition, and surface functional groups of carbon dots. These controlled properties have enabled some studies to achieve selective detection of microplastics.[28] However, their specific role in the photocatalytic degradation process of microplastics has not yet been extensively investigated.

In this study, two of the most representative plastic pollutants were selected as model pollutants: polyethylene terephthalate (PET) is widely used in producing beverage bottles, food packaging and textiles and is considered a primary pollutant in contaminated water bodies.[32] Polylactic acid (PLA) is mainly used in food packaging, disposable tableware, fibers and non-woven fabrics, biomedical applications and 3D printing and possesses a stable chemical structure, leading to very slow degradation rates in natural environments.[33] TiO_2 nanoflowers were synthesized *via* a hydrothermal method, and CQDs were subsequently composited onto the TiO_2 surface using urea and citric acid as precursors. This research aims to investigate the photocatalytic degradation of microplastic samples under pH conditions approximating those of natural water bodies. The effects of CQDs and solution pH on the photocatalytic degradation of microplastics by TiO_2 were systematically investigated, and the potential application of CQDs@TiO_2 composites in the remediation of microplastic pollution was explored.

2. Materials

HCl (Sinopharm Chemical Reagent Co., Ltd), urea (H_2NCONH_2, Tianjin Zhiyuan Chemical Reagent Co., Ltd), citric acid ($C_6H_8O_7 \cdot H_2O$, Sinopharm Chemical Reagent Co., Ltd), tetra-*n*-butyl titanate (98%, Aladdin Biochemical Technology Co., Ltd), absolute ethanol (AR, Xilong Chemical Co., Ltd), Na_2HPO_4 (99%, Aladdin Biochemical Technology Co., Ltd), KH_2PO_4 (99.5%, Aladdin Biochemical Technology Co., Ltd), KOH (AR, Aladdin Biochemical Technology Co., Ltd), PLA (100 mesh,

Taifeng Macromolecular Materials), PET (200 mesh, Hengfa Plastics).

3. Experiment

3.1 Preparation of TiO_2 nanocrystallines

Titanium dioxide was prepared based on a previous study.[34] Titanium dioxide was prepared. The specific process is as follows: 8 g of urea was dissolved in 2 mol/L HCl, followed by the slow dropwise addition of 1 mL tetrabutyl titanate. The mixture was stirred at room temperature for 30 minutes and then transferred into a polytetrafluoroethylene-lined autoclave for a hydrothermal reaction at 120 °C for 30 minutes, 1 hour, 1.5 hours, and 2 hours. After the reaction, the products were centrifuged and washed several times, then dried at 80 °C for 4 hours to obtain white powders. Note: no sample was collected for the 30 min hydrothermal reaction. The resulting samples were labeled as 1h-TiO_2, 1.5h-TiO_2, and 2h-TiO_2, respectively. Finally, the collected samples were calcined at 500 °C for 30 minutes and labeled as 1hTiO_2-500 °C, 1.5hTiO_2-500 °C, and 2hTiO_2-500 °C, respectively.

3.2 Preparation of CQD@TiO_2 composite photocatalyst

1 g of urea and 1 g of citric acid were dissolved in 30 mL of pure water, and the solution was stirred at room temperature for 30 minutes. A mixture of urea (1 g) and citric acid (1 g) was dissolved in 30 mL of deionized water under continuous stirring at room temperature for 30 minutes. Subsequently, 0.054 g of titanium dioxide (TiO_2) powder was introduced into the solution, which was then subjected to ultrasonication for 20 minutes to ensure uniform dispersion of TiO_2. The resulting dispersion was transferred into a Teflon-lined autoclave and hydrothermally treated at 180 °C for 6 hours. After cooling naturally to room temperature, the product was collected through repeated centrifugation and washing. The obtained solid was further immersed in a 0.2 M acetic acid solution for 30 minutes, followed by filtration, washing, and drying at 80 °C for 12 hours, yielding a light-yellow powder.

In order to explore the influence of carbon dot content on the composite, the amounts of urea and citric acid added were adjusted in parallel trials to 0 g, 0.5 g, 1.5 g, and 2 g, respectively.

3.3 Pretreatment of microplastics

1 g of PET or PLA microplastics was added to 10 mL 5 M or 1 M KOH solution, respectively. After ultrasonic dispersion to achieve uniformity, the mixture was stirred at room temperature for 30 minutes and then washed until the washing solution became neutral. The treated sample was dried at 80 °C to obtain alkali-treated microplastics.

3.4 Material characterization and testing

SEM was performed using a Thermo Fisher Quanta 250 FEG scanning electron microscope (USA) with an accelerating voltage of 200 V to 30 kV. EDS mapping analysis was conducted using an Oxford Instruments X-MAX-50 energy dispersive X-ray spectrometer (UK) in area scanning mode. XRD was performed using a Bruker D/MAX-2500 X-ray diffractometer (Rigaku, Japan) with Cu-Kα radiation at a scanning rate of 5°/min, tube voltage of 40 kV, tube current of 40 mA and a diffraction angle range of 10° to 80°. UV-vis absorption spectra were obtained using a UV-1081 ultraviolet-visible diffuse reflectance spectrometer (Beijing Beifen Ruili Analytical Instrument Co., Ltd, China). UV-vis DRS absorption spectra were also obtained using a Shimadzu UV-3600i Plus ultraviolet-visible-near-infrared spectrophotometer (Japan). FTIR analysis was conducted using a Thermo Fisher Scientific Nicolet iS50 Fourier transform infrared spectrometer (USA) with a scanning range of 4000 to 400 cm^{-1}. BET analysis was performed using the SI series high-speed automated surface area and pore size analyzer (Quantachrome Instruments, USA). Electron paramagnetic resonance (EPR) measurements were performed using a Bruker A300emx-plus spectrometer (Germany). Photoluminescence (PL) and time-resolved PL (TRPL) analyses were conducted on an Edinburgh Instruments FLS1000 spectrometer (UK), with a scan range of 300–800 nm, using an excitation wavelength of 340 nm. Transmission electron microscopy (TEM) was conducted on a Hitachi HF5000 (probe aberration-corrected) instrument. X-ray photoelectron spectroscopy (XPS) was performed using a Shimadzu AXIS Ultra DLD X-ray photoelectron spectrometer (Japan). HS-GC-MS was performed using an Agilent 7890 gas chromatograph–mass spectrometer (Agilent Technologies, USA). LC-MS analysis was conducted on a Waters 2695 separation module coupled with a Waters ZQ2000 single quadrupole mass spectrometer equipped with an ESI source.

Photoelectrochemical performance testing: 50 mg of the catalyst was weighed and added to 1 mL of anhydrous ethanol. The mixture was stirred and ultrasonically dispersed to form a suspension. This suspension was then spin-coated onto an FTO glass substrate at 2000 rpm and the coating process was repeated four times. The sample was then dried in an oven at 60 °C.

The testing was conducted under AM 1.5G illumination (100 mW cm^{-2}) using CHI660E electrochemical workstation of Shanghai Chenhua Instrument Co., Ltd. A standard three-electrode system was used, with an Ag/AgCl reference electrode, a Pt wire counter electrode, and the as-prepared TiO_2/CQDs film as the working electrode, immersed in a 0.5 M Na_2SO_4 electrolyte solution. The *I–t* test parameters were set as follows: initial voltage 0 V, data resolution 0.1 s. The light source was manually interrupted every 20 seconds for a duration of 2 seconds.

Electrochemical Impedance Spectroscopy (EIS) measurements were performed using a Zahner ZM6 electrochemical workstation (Germany) under AM 1.5G illumination (100 mW cm^{-2}). A conventional three-electrode system was employed, consisting of an Ag/AgCl electrode as the reference a Pt wire counter electrode, and the as-prepared photocatalyst film as the working electrode. An aqueous solution of 0.5 M Na_2SO_4 was used as the electrolyte.

Degradation of microplastics: a 250 W xenon lamp with an irradiance of 100 mW cm^{-2} was used as the light source. The experimental procedure was as follows: 80 mg of microplastics was added to PBS solutions with pH values of 6.8, 7.4, and 8.0,

respectively, and stir thoroughly to disperse. Then, 80 mg of the catalyst was added. The mixtures were stirred in the dark for 30 minutes to achieve adsorption–desorption equilibrium. The samples were then exposed to the light source for 48 hours under continuous stirring. After degradation, the solid mixture of catalyst and microplastics was collected by centrifugation, washed once with pure water, and dried at 70 °C for 12 hours. The weight loss of the microplastics was calculated using the following formula:

$$\text{Weight loss} = \frac{M_0 - M_{48h}}{M_0} \times 100\%$$

where M_0 (mg) and M_{48h} (mg) are the total mass of the photocatalyst and microplastics before and after 48 hours of irradiation, respectively.

4. Results and discussion

As shown in Fig. 1(a), the powders obtained *via* hydrothermal synthesis all exhibit distinct diffraction peaks at approximately $2\theta = 25.3°$, 37.8°, 48.0°, and 55.1°. These peaks correspond to the (101), (004), (200), and (211) crystal planes of anatase TiO_2, respectively, and match well with the standard reference card PDF#71-1166. This confirms that all the synthesized samples are anatase TiO_2. According to Fig. 1(b) and S1, after calcination at 500 °C, the diffraction peaks of TiO_2 become significantly more intense and sharper, indicating that the annealing treatment improves the crystallinity of TiO_2. The introduction of carbon quantum dots (CQDs) does not cause noticeable changes in the characteristic diffraction peaks of the samples. This could be attributed to the low amount of CQDs present.

Fig. S2 presents the SEM images of the synthesized TiO_2. It can be observed that the TiO_2 consists of irregular nanospheres, each self-assembled from smaller primary particles. This phenomenon is more evident in the TEM micrograph shown in Fig. 2(c). From Fig. S2(a) to (c), it is evident that with a hydrothermal duration of 1 hour, some nanospheres are incomplete and exhibit a rough surface. As the hydrothermal time increases, the nanospheres become more integral, with a reduction in surface roughness. Furthermore, their radius increases, and the size distribution becomes more uniform. Fig. S2(d) to (f) reveal that after calcination, the primary crystallites constituting the nanospheres grow larger and their edges become rounded. However, the nanospheres obtained from 1-hour and 1.5-hour hydrothermal treatments show a certain degree of fracture, and the shorter the hydrothermal time, the more severe the fragmentation appears to be after annealing.

As observed in Fig. 2(a) and (b), after the incorporation of CQDs, the color of the TiO_2 powder changed to a light yellowish-brown, and some of the surface irregularities of TiO_2 were covered by the CQDs. In Fig. 2(d), the lattice spacings of 0.22 nm and 0.35 nm correspond to the (100) plane of graphitic carbon and the (101) plane of anatase TiO_2, respectively. The observable size of the carbon dots is approximately 4.18 nm. The elemental mapping image in Fig. 2(e)–(h) show that the carbon elements are relatively uniformly distributed on the TiO_2 surface. X-ray photoelectron spectroscopy (XPS) measurements were conducted to investigate the elemental composition and chemical states of the as-synthesized CQDs@1hTiO_2 composite. The survey spectrum (Fig. 3(a)) confirms the presence of Ti, O, and C elements in the sample, which is consistent with the expected composition of carbon quantum dots (CQDs) decorated on titanium dioxide and the TEM results. The Ti 2p spectrum (Fig. 3(b)) displays two distinct peaks at binding energies of ~458.5 eV and ~464.3 eV, corresponding to Ti^{4+}. The O 1s spectrum (Fig. 3(c)) is deconvoluted into three peaks at ~529.8 eV, ~531 eV, and ~533.5 eV, assigned to Ti–O bonds, surface hydroxyl groups (O–H), and C–O–C bonds, respectively. The presence of surface hydroxyl groups facilitates the adsorption of organic pollutants and the generation of reactive oxygen species during photocatalysis. The C 1s spectrum (Fig. 3(d)) is fitted with three peaks at ~284.8 eV, ~286.3 eV, and ~288.7 eV, corresponding to C–C, C–O, and Ti–O–C=O species, respectively. The Ti–O–C=O peak provides direct evidence of chemical bonding between CQDs and TiO_2, which promotes efficient

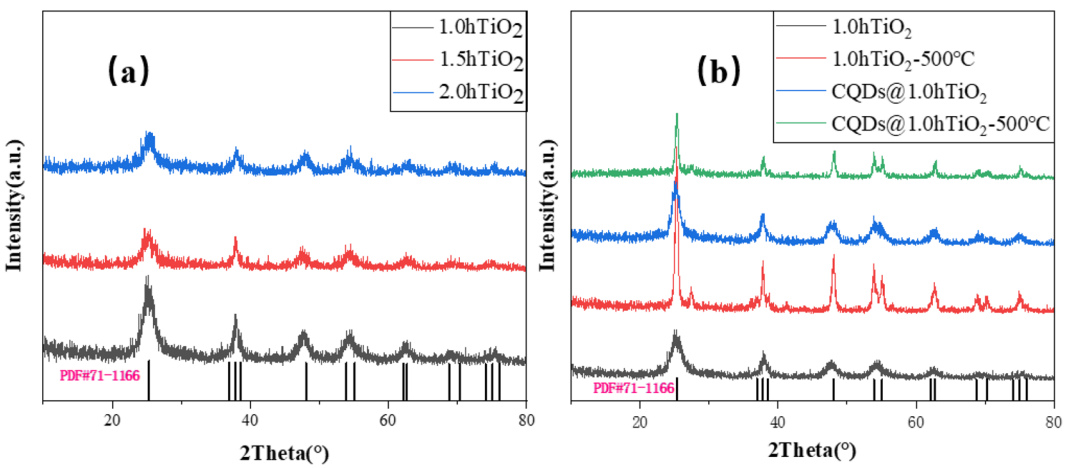

Fig. 1 XRD patterns: (a) unsintered TiO_2; (b) photocatalyst based on 1hTiO_2.

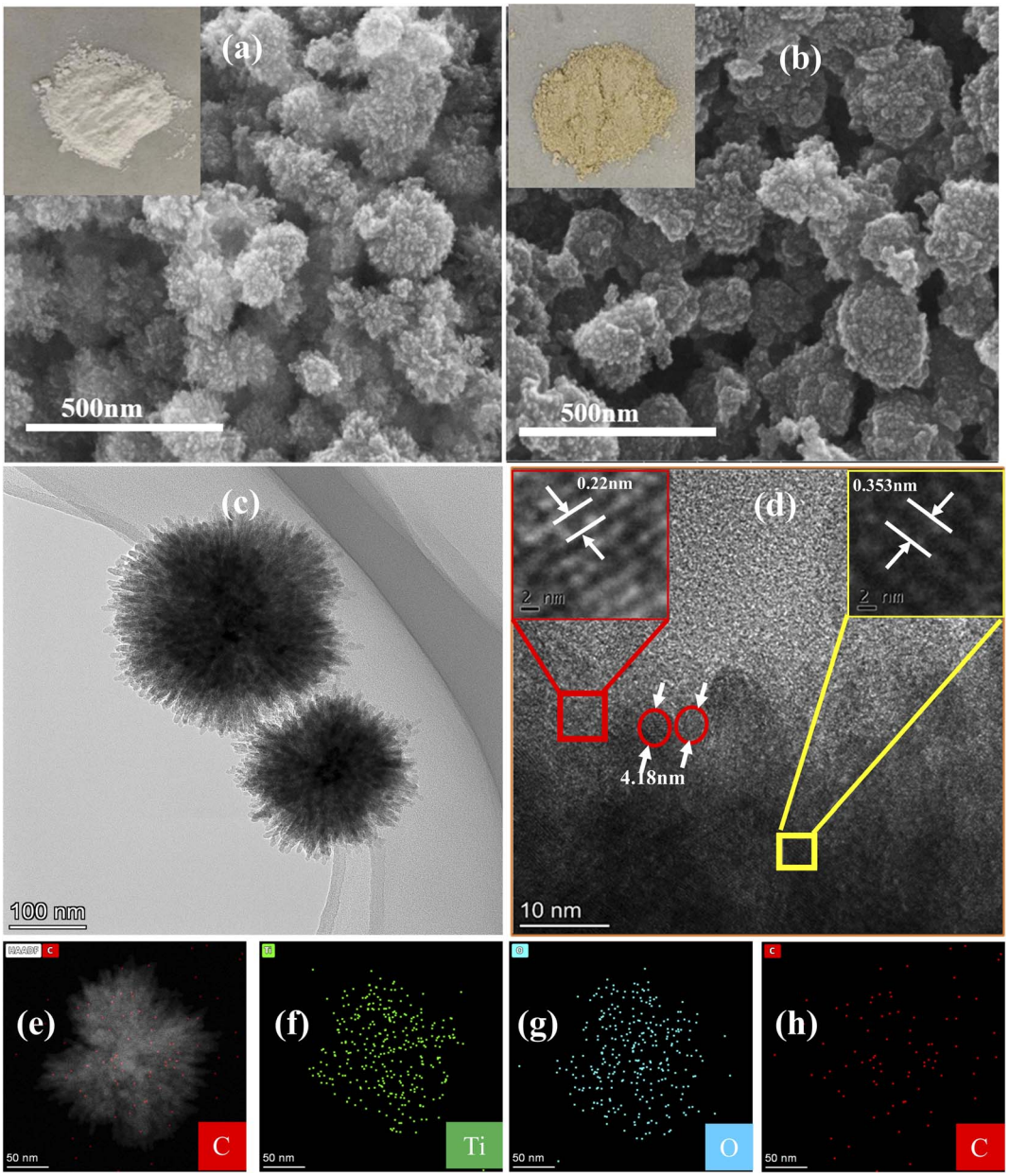

Fig. 2 (a) SEM image of 1hTiO$_2$ (inset shows a physical photograph); (b) SEM image of CQDs@1hTiO$_2$ (inset shows a physical photograph); (c) and (d)TEM image of CQDs@1hTiO$_2$; (e) HAADF-STEM image of the composite and the corresponding. EDS elemental mappings of (f) Ti, (g) O, and (h) C (overlay).

interfacial charge transfer and enhances photocatalytic performance. Furthermore, these results indicates that the carbon dots have successfully been loaded onto the TiO_2.

To evaluate the photocatalytic performance of the as-synthesized samples, Rhodamine B (RhB) was degraded under light irradiation using the prepared materials as photocatalysts. For quantitative analysis, the linear relationship between RhB concentration and absorbance was first established (Fig. S3(d)). The degradation results are presented in Fig. S3(a)–S3(c) and Tables S1–S2. As is well known, the characteristic absorption peak of RhB at 554 nm originates from the conjugated chromophore in its molecular structure. The results show that only 6.62% of RhB was degraded after 30 min of light irradiation in the absence of a photocatalyst. In contrast, with the addition of the photocatalysts under identical conditions, the peak intensity at 554 nm decreased markedly for all samples, and some exhibited a blue shift. These findings confirm that all prepared samples possess photocatalytic activity and promote the photodegradation of RhB.

Additionally, the loading amount of carbon dots was optimized by adjusting the concentration of the carbon source. As shown in Fig. S3(c) and Table S2, the composite exhibited the best catalytic performance when the mass of citric acid was 1 g (corresponding to 0.17 M). Furthermore, the photocatalytic

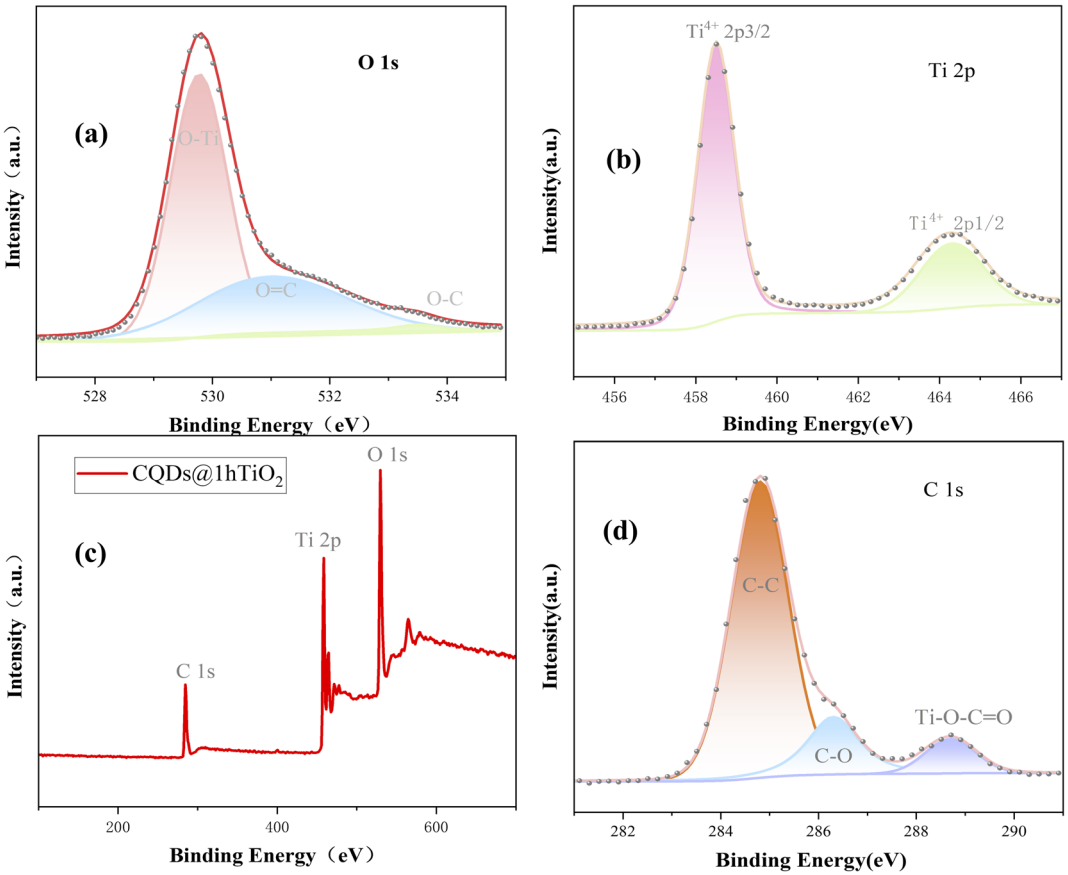

Fig. 3 (a) XPS survey spectrum of the CQDs@TiO_2 sample; high-resolution XPS spectra of (b) Ti 2p; (c) O 1s and (d) C 1s.

performance of TiO_2 decreased with increasing hydrothermal duration, likely due to changes in particle size and specific surface area. Annealing treatment enhanced the photocatalytic activity of TiO_2, owing to its improved crystallinity. The improved crystallinity reduces deep-level recombination centers (*e.g.*, vacancies and dislocations) within the lattice, thereby providing a more continuous transport pathway for charge carriers. Additionally, the highly crystalline TiO_2 surface facilitates the exposure of active facets such as (001).[35,36] When the carbon source loading was fixed at 1 g, the incorporation of CQDs significantly boosted the photocatalytic performance of non-annealed TiO_2. However, among the annealed TiO_2 samples, only CQDs@1hTiO_2-500 °C showed enhanced activity. This may be attributed to the reduction of surface functional groups and defects on TiO_2 after calcination, which weakens the interaction with CQDs. Among all the samples, CQDs@1hTiO_2 exhibited the best photocatalytic performance and was therefore selected for further detailed investigation. This may be because the carbon dots themselves possess excellent light absorption capability, acting as an "antenna" that transfers the absorbed light energy to TiO_2, thereby indirectly broadening the composite's light response range. Additionally, the formation of Ti–O–C chemical bonds (Fig. 3(d)) introduces impurity levels or intermediate energy states. These new energy levels are typically located between the valence and conduction bands of titanium dioxide, allowing electrons to be excited in a "stepwise" manner—first transitioning to the intermediate energy level and then to the conduction band. Effectively, the total energy required is reduced, which macroscopically manifests as a narrowing of the bandgap.[37,38]

Fig. 4(a) presents the UV-vis DRS spectra of 1hTiO_2 and CQDs@1hTiO_2. The corresponding Tauc plots were drawn based on the Tauc equation, and their band gaps were calculated (Fig. 4(b)). The modification with CQDs caused a noticeable red-shift in the absorption edge of 1hTiO_2, reducing the band gap from 3.0 eV to 2.8 eV. Fig. 4(c) and (d) illustrates the influences of CQDs on the specific surface area and porosity of TiO_2, with relevant results listed in Table 1. Before CQDs modification, the BET specific surface area of 1hTiO_2 was 311.74 $m^2\ g^{-1}$. The adsorption–desorption isotherm exhibited only a subtle hysteresis loop (H3-type) in the high-pressure region, making it more closely resemble a Langmuir type II isotherm. This is consistent with the morphology where small 1hTiO_2 particles self-assemble into larger aggregates, which then stack loosely (as shown in Fig. 2(b) and (c)). The pore size distribution indicates a broad range for 1hTiO_2, spanning from micropores of a few nanometers to macropores up to 100 nm. The micropores primarily exist between the self-assembled primary particles, while the macropores form from the stacking of the larger aggregates. After modification with CQDs, the

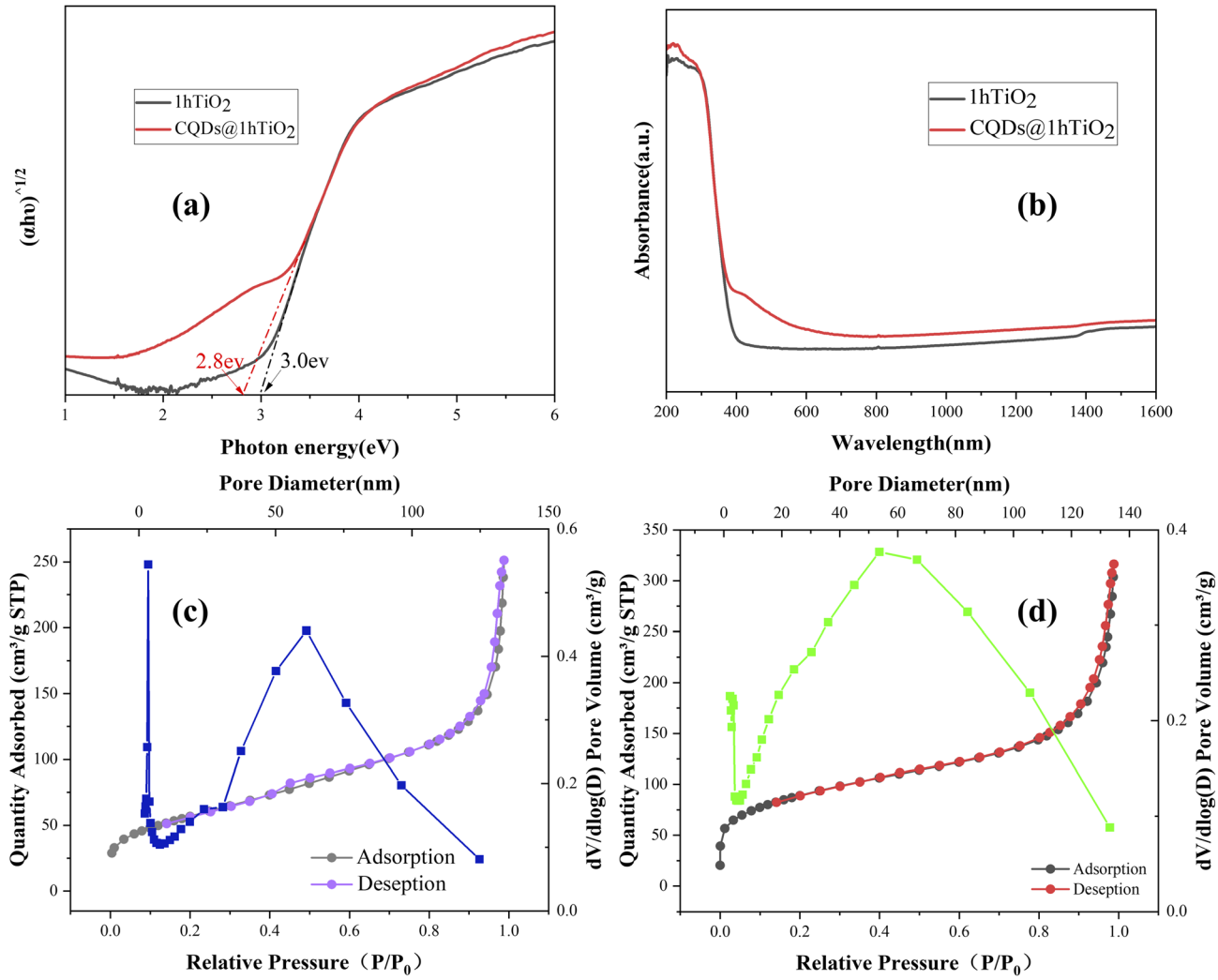

Fig. 4 (a) UV-vis DRS spectra of $1hTiO_2$ and $CQDs@1hTiO_2$; (b) the corresponding band gaps of $1hTiO_2$ and $CQDs@1hTiO_2$. N_2 adsorption–desorption isotherms and the average pore size distribution of the catalyst materials: (c) $1hTiO_2$; (d) $CQDs@1hTiO_2$.

Table 1 The physical properties of as-prepared samples

Samples	S_{BET} ($m^2\ g^{-1}$)	*t*-Plot micropore area ($m^2\ g^{-1}$)	Pore volume ($cm^3\ g^{-1}$)	Average pore size (nm)
$1hTiO_2$	311.7354	54.1858	0.489299	6.2784
$CQDs@1hTiO_2$	205.1570	7.6202	0.388532	7.5753

specific surface area of $CQDs@1hTiO_2$ decreased to 205.16 $m^2\ g^{-1}$. The overall shape of the adsorption–desorption isotherm for $CQDs@1hTiO_2$ remained similar to that of the unmodified sample, but a small hysteresis loop appeared in the medium-pressure region, characteristic of mesoporous materials. This suggests that the introduction of CQDs increased the mesoporosity of $1hTiO_2$, which aligns with the pore size distribution curve (Fig. 4(d)). Based on this analysis, the addition of CQDs reduced the specific surface area of $1hTiO_2$ but increased its mesoporous content, likely due to the growth of CQDs filling some of the original voids.

Fig. 5(a) shows the recorded *I*–*t* curves under intermittent ON-OFF cycles with 100 mW cm^{-2} irradiation. Clearly, a higher and more stable photocurrent density with less decay was obtained for $CQDs@1hTiO_2$. This indicates that the incorporation of CQDs significantly enhanced the photoresponse of $1hTiO_2$, which is consistent with the reduced band gap of $CQDs@1hTiO_2$.

EIS was employed to investigate the interfacial charge transfer behavior of $1hTiO_2$ and $CQDs@1hTiO_2$ during the photocatalytic reaction. As shown in Fig. 5(b), the dots represent the experimental data, the solid lines represent the fitted data,

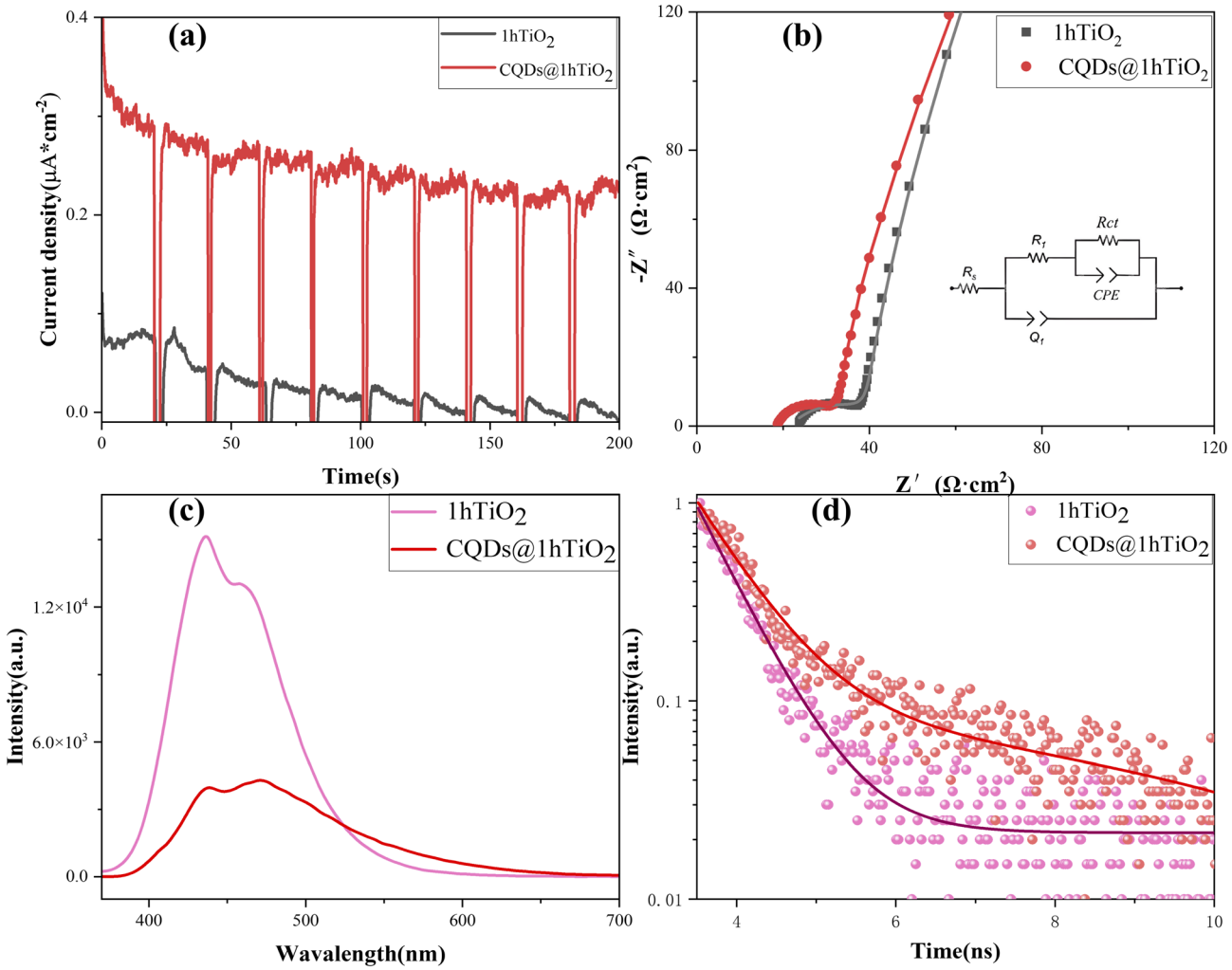

Fig. 5 (a) $I-t$ curves of $1hTiO_2$ and $CQDs@1hTiO_2$; (b) the electrochemical impedance spectra of $1hTiO_2$ and $CQDs@1hTiO_2$; (c) PLspectrum of $1hTiO_2$ and $CQDs@1hTiO_2$; (d) TRPL spectrum of $1hTiO_2$ and $CQDs@1hTiO_2$.

and the inset shows the equivalent circuit (the corresponding fitting parameters are presented in Table 2). Rs represents the solution resistance, corresponding to the high-frequency intercept of the curve with the real axis (Z'). It is independent of the electrode material. The semicircles in the high-frequency region of the two curves correspond to the charge transfer resistance R_{ct} at the electrode/electrolyte interface, and their diameters directly reflect the separation and migration efficiency of photogenerated carriers. Comparison shows that the pure $1hTiO_2$ has a larger R_{ct} (22.37 Ω cm^2), indicating that its photogenerated electron–hole pairs are prone to recombination with high charge transfer resistance.[39] In contrast, the R_{ct} of $CQDs@1hTiO_2$ is significantly reduced to 13.55 Ω cm^2, demonstrating that the introduction of CQDs, as a "charge transport bridge", effectively promotes the separation and migration of photogenerated carriers, reduces the probability of charge recombination, and thus improves the photocatalytic performance of the material. R_1 is related to the charge transport capability within the material.[40] After the addition of CQDs, the value of R_1 decreased from 5741 Ω cm^2 to 4648 Ω cm^2, indicating that CQDs facilitate the charge migration within the photocatalytic material.

Table 2 Statistical analysis of ESI and TPPL fitting data of photocatalysts

Catalyst	R_s (Ω cm^2)	R_{ct} (Ω cm^2)	R_1 (Ω cm^2)	Carriers life time(ns) τ_1	τ_2
$IhTiO_2$	21.68	22.37	5741	0.47	2.99
$CQDs@1hTiO_2$	18.84	13.55	4648	0.53	3.21

In Fig. 5(c) and (d), PL and TRPL spectroscopy were employed to evaluate the photogenerated carrier dynamics of $1hTiO_2$ and $CQDs@1hTiO_2$. As shown in Fig. 5(c), the PL peak intensity of $CQDs@1hTiO_2$ is significantly lower than that of pure $1hTiO_2$, indicating that the introduction of CQDs effectively suppresses the recombination of photogenerated

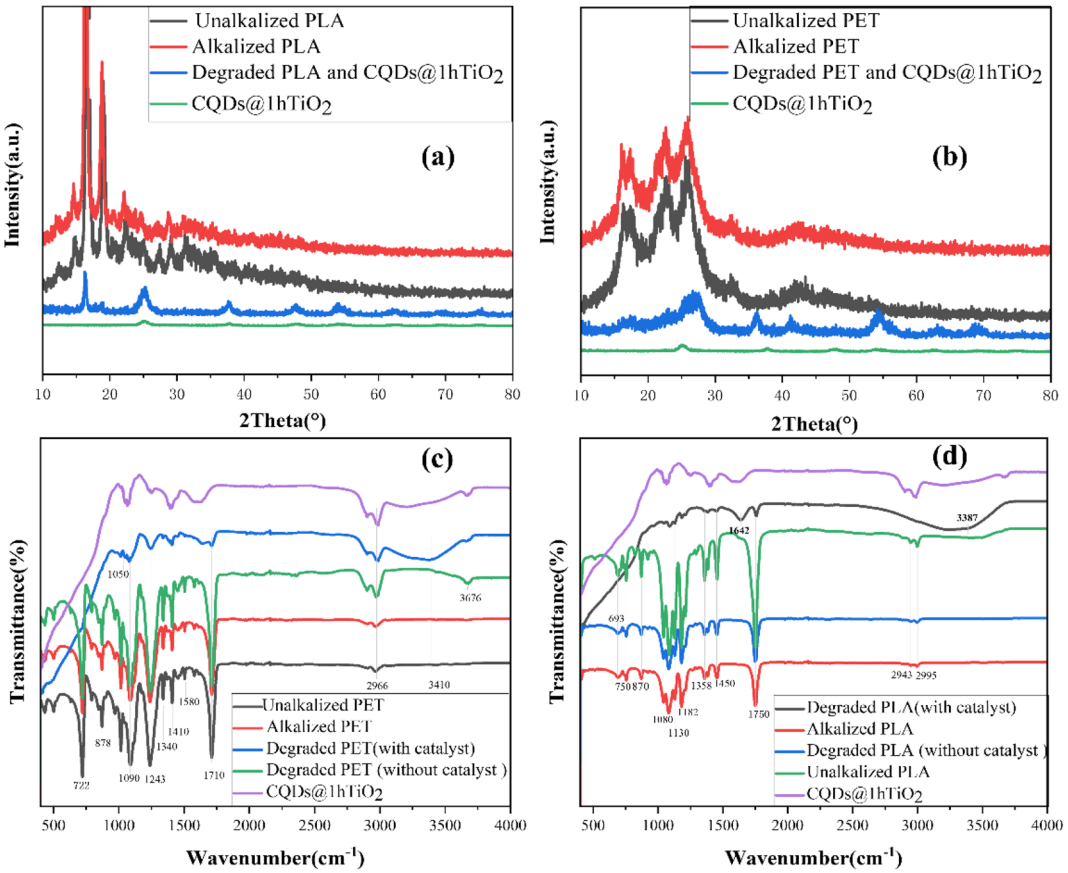

Fig. 6 (a) XRD patterns of PET microplastics; (b) XRD patterns of PLA microplastics; (c) FTIR spectra of PET and CQDs@1hTiO$_2$; (d) FTIR spectra of PLA and CQDs@1hTiO$_2$ (all microplastics subjected to degradation in the figure were alkali-treated, and degradation was conducted in PBS buffersolution at pH 8.0).

electron–hole pairs. The TRPL decay curves were fitted with a biexponential function $I(t) = A_1e^{-t/\tau_1} + A_2e^{-t/\tau_2}$, yielding a short lifetime τ_1 and a long lifetime τ_2 (Table 2). τ_1 is attributed to fast non-radiative recombination at defect sites, while τ_2 corresponds to slow radiative recombination or charge transfer process. Compared with 1hTiO$_2$, both τ_1 and τ_2 of CQDs@1hTiO$_2$ are prolonged, demonstrating higher separation efficiency of its photogenerated carriers. This is consistent with the reduced charge transfer resistance observed in the electrochemical impedance spectra, collectively confirming the crucial role of CQDs in promoting charge separation and transport.

Based on the aforementioned analysis, although the addition of CQDs slightly reduces the specific surface area, it broadens the light response range of the material, effectively promotes the separation and migration of photogenerated carriers, increases carrier lifetime, reduces the probability of charge recombination, and thus significantly enhances the photocatalytic performance.

The degradation of microplastics is extremely difficult; therefore, this study employed a 5 M KOH solution to pretreat PET and PLA microplastics before degradation. As shown in Fig S4, after strong alkali treatment, the surface of PET microplastic particles became corroded and rough, with numerous wrinkle-like textures appearing. In contrast, the corrosion on the surface of PLA particles was more severe, presenting a floc-like morphology after alkali treatment. According to Fig. 6(a) and (b), distinct diffraction peaks were observed for both untreated and alkali-treated PET at 2θ values of 17°, 22.5°, and 25.5°. Similarly, for both untreated and alkali-treated PLA, a strong and sharp peak appeared near 16.7°, along with strong diffraction peaks at 19.1° and 22.4°. These findings are consistent with previously reported characteristic diffraction peaks of PET and α-crystalline PLA,[41–44] with no significant changes in the diffraction peaks. Additionally, in the infrared spectra of Fig. 6(c) and (d), the characteristic peaks of PET and PLA showed no notable changes before and after alkali treatment, indicating that the main functional groups in these two types of microplastics remained almost unchanged. These results suggest that alkali treatment does not directly degrade PET and PLA; however, it leads to partial cleavage of ester bonds on the material surface, increasing surface defects or cracks. These defects and cracks facilitate contact with catalysts and make the microplastics more susceptible to attack by subsequent oxidants or active pecies, ultimately accelerating polymer chain breakage and improving degradation efficiency. This is further supported by the results in Fig. 7 and Table 3. Under the

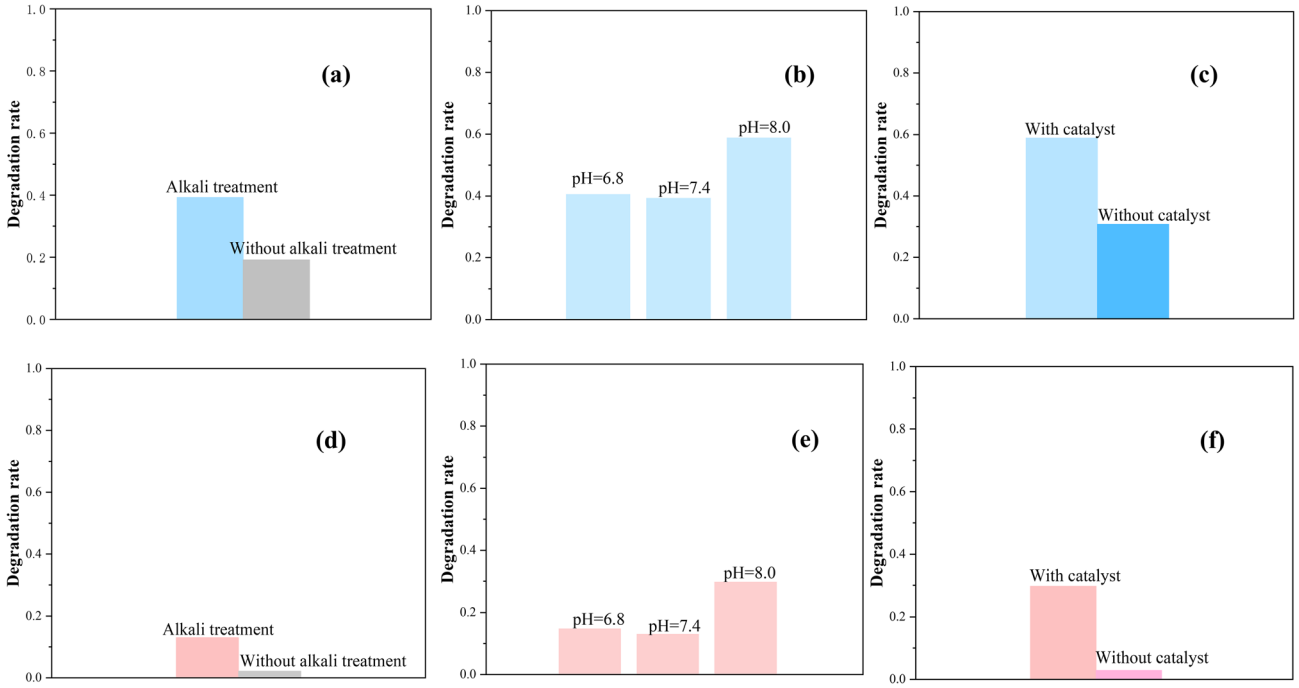

Fig. 7 (a)–(c) Bar graphs of degradation rates for different PET samples after 48-hour degradation; (e) and (f) bar graphs of degradation rates for different PLA samples after 48-hour degradation ((a) and (e) were obtained from degradation in PBS buffer at pH 6.8; (c) and (f) were obtained from degradation in PBS solution at pH 8.0).

same conditions, alkali treatment increased the degradation rates of PET and PLA by 513% and 105%, respectively.

Since the natural environment is predominantly neutral, the degradation experiments in this study were conducted at pH levels of 6.8, 7.4, and 8.0. The corresponding degradation rates, calculated based on mass change are presented in Fig. 7 and Table 3. The results indicate that under identical conditions, the degradation rates of both plastics remained relatively low in the absence of a photocatalyst. This observation is further supported by the FTIR spectra in Fig. 6(c) and (d), which show almost no differences between the samples before and after degradation.

The pH of the solution environment also influenced the degradation of the two microplastics. The highest degradation degree for both PET and PLA, 29.8% and 58.9% respectively, was achieved in a slightly alkaline buffer solution. This could be attributed to the fact that both PET and PLA are ester-based polymers. Although the alkaline environment is unfavorable for the adsorption of CQDs@TiO_2 on microplastics, it can promote the attack of reactive species on ester bonds, making them easier to cleave. Between these two opposing effects, the promoting effect is greater, thereby accelerating the degradation of PET and PLA. Fig. 8 shows the SEM images of the alkali-treated microplastics before and after 48 hours of degradation in a PBS solution at pH 8.0. The images reveal that most of the undegraded PET after 48 h had become smaller or even fragmented, as seen in Fig. 8(b). This fragmentation was more pronounced in the PLA samples, where almost no intact PLA particles remained after 48 h degradation, as shown in Fig. 8(d). From the XRD patterns in Fig. 6(a) and (b), it can be observed that after 48 hours of degradation in pH 8.0 PBS solution, the characteristic diffraction peaks of both alkali-treated PET and PLA significantly decreased. This is related to random bond scission within the polymer, wheremolecular chains in the crystalline regions are cleaved, disrupting the originally ordered structures. Meanwhlie, the newly emerged diffraction peaks belong to the anatase titanium dioxide catalyst.

In the FTIR spectrum of alkali-treated PET 48 hours after degradation (Fig. 6(c)), the absorption peaks at 722 cm^{-1}, 878 cm^{-1}, and 1340 cm^{-1} disappeared, while the intensities of the peaks at 1090 cm^{-1}, 1243 cm^{-1} , and 1710 cm^{-1} decreased substantially. A broad peak and a weak peak emerged at 3410 cm^{-1} and 1050 cm^{-1}, respectively. The significant reduction of the peak at 1710 cm^{-1}, assigned to the C=O stretching vibration of the aromatic ester, resulted from the cleavage of the core ester bonds in PET, leading to a decrease in ester groups and the formation of carboxylic acid C=O. The peaks at 1243 cm^{-1} and 1090 cm^{-1}, corresponding to the asymmetric C–O–C stretching of the aromatic ester and the O–CH_2 stretching vibration, respectively, provide further evidence of ester bond cleavage. The appearance of the broad peak at 3410 cm^{-1} is attributed to O–H stretching vibrations of hydroxyl groups bonded by hydrogen bonds, associated with the generation of carboxylic acids (–COOH) and alcohols (–OH) from ester bond cleavage during oxidative degradation. This serves as definitive evidence of degradation. The weak peak at 1050 cm^{-1} belongs to the C–O stretching vibration of alcohols, indicating that some PET underwent oxidation. Furthermore, the disappearance of the characteristic peaks at 722 cm^{-1} and 878 cm^{-1}, assigned to the out-of-plane bending vibrations of C–H of the

Table 3 Statistical table of microplastic degradation after 48 h under 100 mW cm^{-2} visible light irradiation

Microplastic	Alkali treatment	Catalysts	pH	Initial weight (mg)	Weight after degradation (mg)	Degradation rate (%)
PET	With	CQDs@1hTiO$_2$	8.0	80	56.2	29.8
	With	CQDs@1hTiO$_2$	7.4	80	69.6	13.0
	With	CQDs@1hTiO$_2$	6.8	80	68.2	14.8
	With	No	8.0	80	77.7	2.87
	Without	CQDs@1hTiO$_2$	7.4	80	78.3	2.12
PLA	With	CQDs@1hTiO$_2$	8.0	80	32.9	58.9
	With	CQDs@1hTiO$_2$	7.4	80	48.6	39.2
	With	CQDs@1hTiO$_2$	6.8	80	47.6	40.5
	With	No	8.0	80	55.4	30.8
	Without	CQDs@1hTiO$_2$	7.4	80	64.7	19.1

benzene ring in the phthalic acid unit and two isolated hydrogens on such rings, respectively, indicates that the terephthalate units were converted into free small molecules, causing a drastic change in the benzene ring environment and destruction of the polymer crystal structure.

In Fig. 6(d), comparing the FTIR spectra of PLA before and after degradation shows the disappearance of peaks at 870 cm^{-1}, 750 cm^{-1}, and 693 cm^{-1}, along with a significant decrease in the intensities of the characteristic absorption peaks at 1760 cm^{-1}, 1182 cm^{-1}, and 1080 cm^{-1}. New absorption peaks appeared at 3387 cm^{-1} and 1642 cm^{-1}. The disappearance of the peak at 870 cm^{-1} and the substantial weakening of the peak at 1760 cm^{-1} signify large-scale cleavage of the ester bonds in the PLA backbone, indicating widespread disruption of the integrity of the ester linkages themselves. The disappearance of the peaks at 750 cm^{-1} and 693 cm^{-1} is due to collapse of the polymer backbone, loss of conformation and changes in the local chemical environment, resulting from ester bond cleavage. The reduced intensity of the absorption peaks at 1450 cm^{-1} and ~1358 cm^{-1}, related to the side-chain methyl groups (–CH_3), provides strong evidence for the disruption of the PLA side-chain environment. The appearance of new, broad peaks at 3387 cm^{-1} and 1642 cm^{-1} indicates that some degradation products contain hydroxyl/carboxyl groups or exist in the form of carboxylate salts.

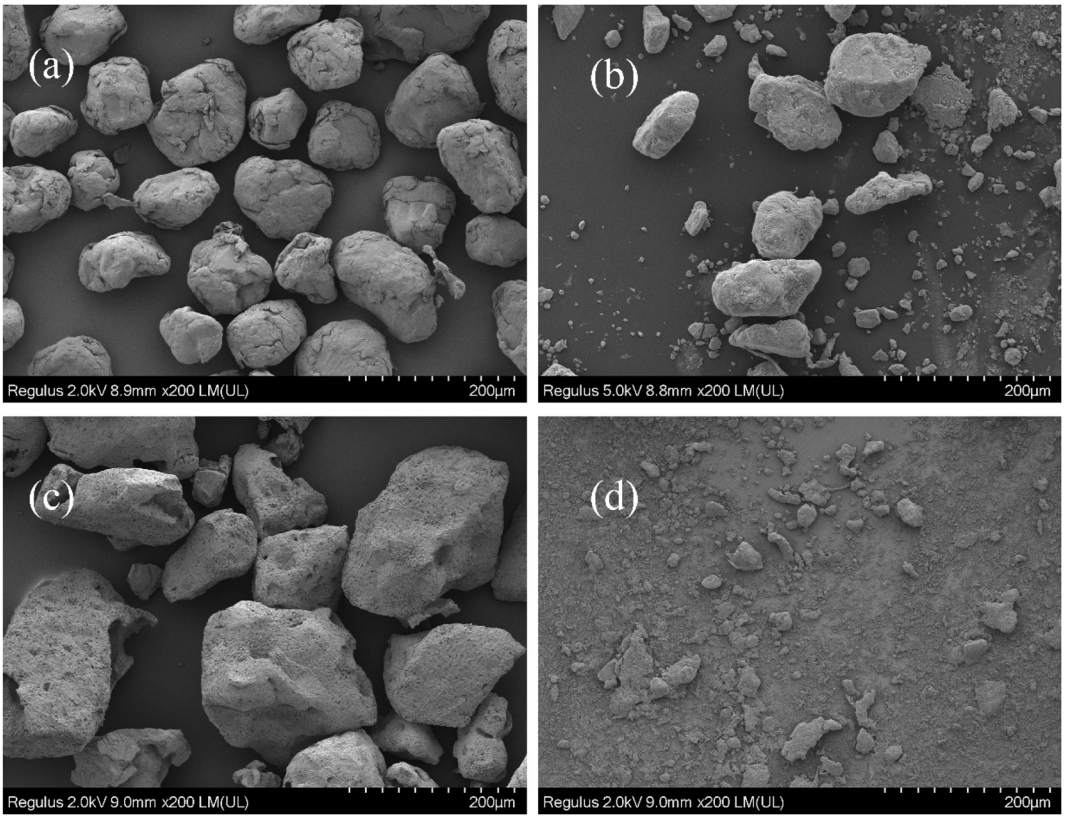

Fig. 8 SEM images of alkali-treated microplastics before and after 48-hour degradation in PBS solution at pH 8.0: (a) PET before degradation; (b) PET after degradation; (c) PLA before degradation; (d) PLA after degradation.

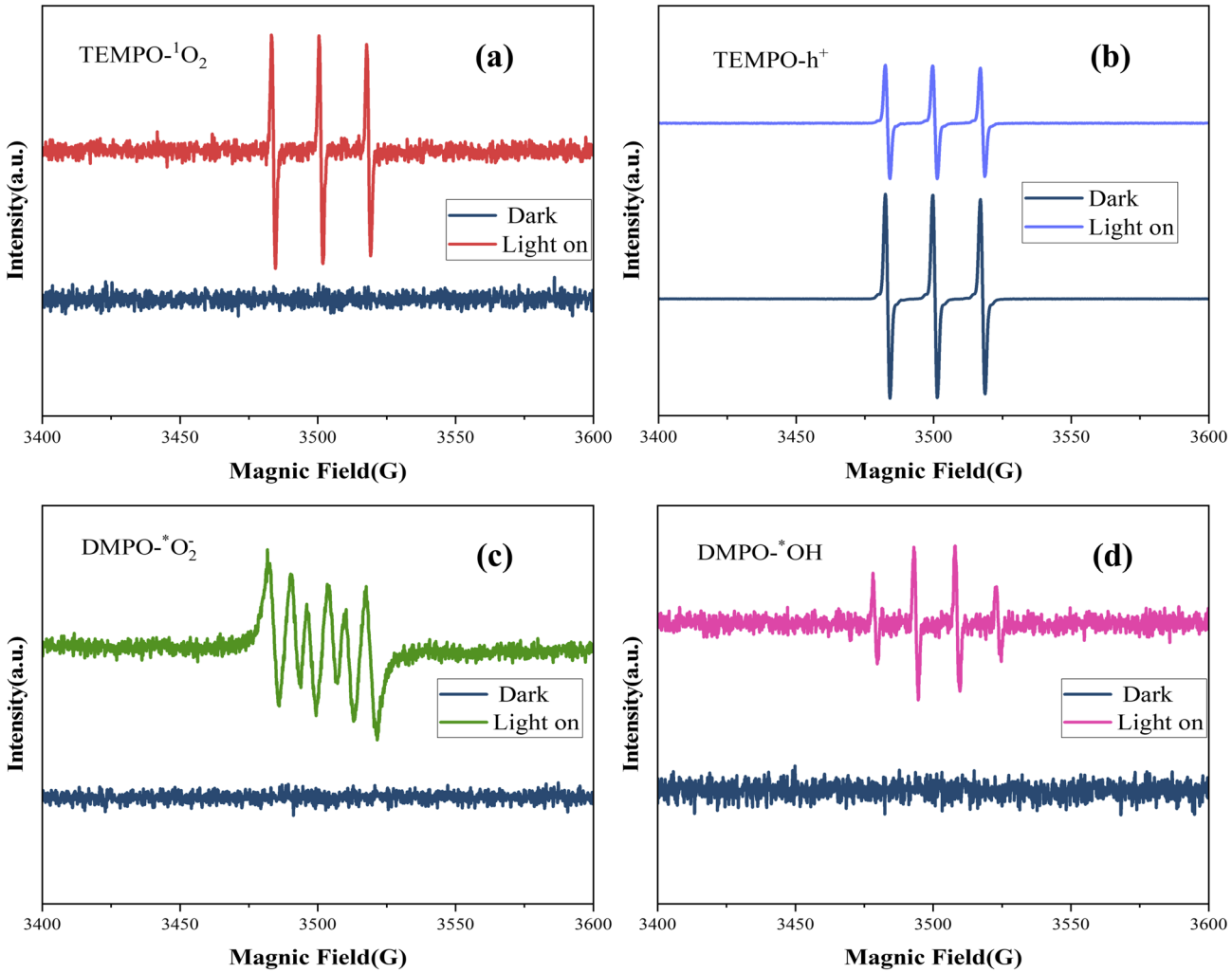

Fig. 9 EPR signals of (a) TEMPO-$^1O_2$; (b) TEMPO-h^+; (c) DMPO-$^*O_2^-$; and (d) DMPO-*OH of CQDs@1hTiO$_2$ in the dark and under AM 1.5G irradiation.

To further identify the degradation intermediate products of PET and PLA, the supernatant after 48 h of degradation was separated and subjected to LC-MS and HS-GC-MS analysis. In LC-MS, the mass spectrometry detection was performed to positive ion mode (ESI$^+$, smoothing (moving average, 2 × 3)) and negative ion mode (ESI$^-$, smoothing (moving average, 2 × 2)); UV detection was performed at two characteristic wavelengths of 214 nm and 254 nm (smoothing (moving average, 2 × 3)). HS-GC-MS analysis was conducted using a GC-MS QP2010 SE (EI source) for signal-to-noise ratio testing, based on total ion chromatogram (TIC) detection, analyzing components detected within the 0–50 min range.

Under LC-MS analysis, a total of 10 characteristic chromatographic peaks were identified for the PET sample (Fig. S5), with corresponding main data listed in Table S3. The main detected intermediates include benzoic acid, benzoate anion, mono(2-hydroxyethyl) terephthalate, ethylene glycol oligomers and terephthalic acid dimer fragments (Fig. S6). In the HS-GC-MS analysis, the PET sample exhibited a TIC value of 16,029,979 (Fig. S10(a)). The detected volatile components included nitrogen, water, ethanol, acetone, ethyl acetate, and various siloxane derivatives (Table S5). Among these, nitrogen and water were identified as matrix components, siloxane derivatives as background interference, and ethanol, acetone, and ethyl acetate as the primary degradation products of PET. For the PLA sample, LC-MS analysis identified 11 characteristic chromatographic peaks (Fig. S7), with corresponding main data presented in Table S4. The main detected intermediates included lactic acid monomers, oxidized lactic acid derivatives, and lactic acid oligomers/polymers (Fig. S8–S9 and Table S4). In the HS-GC-MS analysis, the PLA sample yielded a TIC value of 15,759,315 (Fig. S10(b)). The detected volatile components comprised nitrogen, water, acetaldehyde, ethanol, ethyl acetate, and oligomeric siloxanes (Table S5). Among these, acetaldehyde, ethanol, and ethyl acetate were identified as degradation products of PLA. These findings indicate the breakage of ester bonds and the collapse of molecular structures in PET and PLA, which are consistent with the XRD and FTIR results.

To clarify the catalytic reaction process, photoactive species of CQDs@1hTiO$_2$ were detected, and quenching experiments were conducted on the reactive species. The electron paramagnetic resonance (EPR) spectroscopy was employed to

identify the reactive oxygen species (ROS) and photogenerated holes (h^+) generated under visible-light irradiation. As depicted in Fig. 9(a), the TEMPO spin-trapping experiment revealed the formation of singlet oxygen ($^1O_2$). Notably, a distinct signal was detected only under light illumination, while no observable signal was present in the dark, confirming the light-induced generation of $^1O_2$. In contrast, the TEMPO-h^+ trapping experiment (Fig. 9(b)) exhibited a different behavior. A strong, well-defined signal was observed in the dark, which significantly decreased in intensity upon light irradiation. This phenomenon can be attributed to the reduction of the $TEMPO^+$ radical cation (formed in the dark *via* oxidation by surface defects or residual oxidizing sites) by photogenerated electrons (e^-) under illumination, thereby providing indirect evidence for the production of h^+.[45] For the detection of superoxide anion radicals ($*O_2^-$) and hydroxyl radicals (*OH), DMPO was used as the spin trap. As shown in Fig. 9(c), the characteristic six-line EPR signal of the DMPO-$*O_2^-$ adduct was clearly observed under light irradiation, while it was absent in the dark. Similarly, the four-line spectrum characteristic of the DMPO-*OH adduct was detected only under light-on conditions (Fig. 9(d)). These results directly confirm the light-driven generation of $*O_2^-$ and *OH. In summary, the EPR results collectively demonstrate that under visible-light irradiation, the photocatalytic system simultaneously generates multiple reactive species, including $^1O_2$, h^+, $\cdot O_2^-$, and *OH. These species are proposed to act as the primary oxidizing agents, driving the photocatalytic reaction through multiple pathways.

A series of quenching experiments were also conducted using *p*-benzoquinone (PBQ), L-histidine, ammonium oxalate (AO), and isopropanol (IPA) as quenchers for $*O_2^-$, $^1O_2$, h^+, and *OH, respectively.[46,47] As can be seen from Table 4, the photocatalytic degradation efficiency decreased significantly upon the addition of the quenchers, with the most pronounced effects observed for h^+ and *OH. Based on the above experimental results, it can be concluded that the degradation is attributed to the combined action of $O_2^{\cdot-}$, $^1O_2$, h^+, and *OH. Among them, h^+ and *OH (derived from holes) played a more significant role.

Therefore, the degradation process of both types of ester-based microplastics centers on the hydrolysis of ester bonds.

Table 4 Photocatalytic degradation statistics of microplastics in pH 8 PBS buffer after 48 h with quencher addition

Sample	Quencher	Initial weight (mg)	Weight after degradation (mg)	Degradation rate (%)
PET	PBQ	80	64.8	19.0
PET	L-histidine	80	70.4	12.0
PET	AO	80	74.8	6.50
PET	IPA	80	75.5	5.62
PLA	PBQ	80	48	40.0
PLA	L-histidine	80	58.7	26.6
PLA	AO	80	65.9	17.6
PLA	IPA	80	68.1	14.9

Under the combined action of reactive species such as $^1O_2$, h^+, $\cdot O_2^-$, and *OH, the main chains are broken, the supramolecular structures are disrupted, and short molecular chains, oligomers, or even monomers are generated. These small molecules are ultimately completely mineralized by hydroxyl radicals and other oxidizing agents. The specific process is as follows:[48–50]

$$TiO_2 + h\nu \rightarrow 1TiO_2^* \rightarrow 3\ TiO_2^* \rightarrow TiO_2 + e^- + h^+ \quad (1)$$

$$h^+ + OH^- \rightarrow *OH;\ e^- + O_2 \rightarrow *O_2^- \quad (2)$$

$$h^+ + *O_2^- \rightarrow 1O_2;\ *OH + *O_2^- \rightarrow OH^- + 1O_2;\ O_2^- + H_2O \rightarrow HOO* + OH^- \quad (3)$$

$$2HOO* \rightarrow H_2O_2 + O_2 \quad (4)$$

$$H_2O_2 + e^- \rightarrow *OH + OH^- \quad (5)$$

*OH/h^+/$1O_2$/$*O_2^-$+ terephthalic acid/ethylene glycol/ PET oligomers
→ ethanol, acetone, ethyl acetate, *etc.*
→ CO_2 + H_2O
*OH/h^+/$1O_2$/$*O_2^-$+ lactic acid oligomers/lactic acid
→ acetaldehyde, ethanol, ethyl acetat, *etc.*
→ CO_2 + H_2O (7)

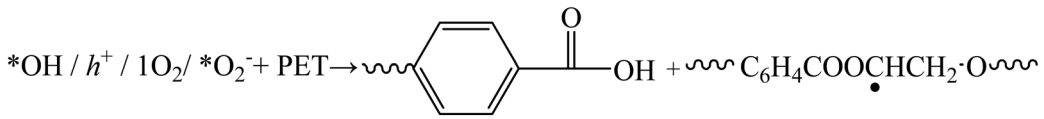

(6)

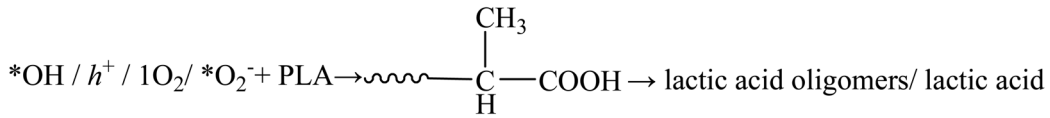

5. Conclusions

This study successfully prepared anatase TiO_2 nanospheres with self-assembling characteristics *via* a simple hydrothermal method. The photocatalytic capability of the resulting material was evaluated, and its potential application in the field of microplastic degradation was explored. The research indicates that the photocatalytic performance of TiO_2 is related to its particle radius, crystalline state and surface modifications. Carbon quantum dots (CQDs) effectively formed composites with the as-synthesized TiO_2 nanospheres (without annealing). Although this composite reduced the specific surface area of TiO_2, it concurrently lowered the bandgap energy, enhanced the material's photoresponsiveness, promoted charge transport within the catalyst and at its interfaces, and reduced the non-radiative recombination of charge carriers, ultimately improving the overall photocatalytic performance. Using commercial PET and PLA as model microplastics, samples were pretreated with a KOH solution. Photocatalytic degradation tests were then conducted using CQDs@1h TiO_2 as the catalyst under 100mW/cm^2 visible light irradiation in a near-neutral PBS solution. The optimal degradation efficiency was observed at pH 8, achieving degradation rates of 28.9% for PET and 59.8% for PLA. The analysis indicates that both types of microplastics underwent a hydrolysis degradation process centered on ester groups, driven by the combined action of $O_2^{\bullet-}$, $^1O_2$, h^+, and *OH. This process involved the formation of short polymer chains, oligomers, monomers, and smaller molecules, which were ultimately completely mineralized into carbon dioxide and water. These results confirm the potential application of quantum dots/titanium dioxide composites for the degradation of microplastics under visible light.

Conflicts of interest

There are no conflicts to declare.

Data availability

Data for this article, including [SEM, XRD, UV-VIS, I-T, BET, FTIR, XPS, TEM, PL, EIS, MS, *etc.*] are available at [Science Data Bank] at [URL-format https://doi.org/10.57760/sciencedb.34829].

Supplementary information (SI): additional figures (Fig. S1–S10) and tables (Tables S1–S5) supporting the analysis presented in the main text. See DOI: https://doi.org/10.1039/d6ra00096g.

Acknowledgements

The authors gratefully acknowledge the financial supporting by National Natural Science Foundation of China (No. 52206232, No. 52402224); Changzhou Sci&Tech Program, China (No. CJ20241094).

References

1 E. Marcharla, S. Vinayagam, L. Gnanasekaran, *et al.*, Sundaram Thanigaivel, Swamynathan Ganesan, Microplastics in marine ecosystems: A comprehensive review of biological and ecological implications and its mitigation approach using nanotechnology for the sustainable environment, *Environ. Res.*, 2024, **256**, 119181.
2 N. Ali, M. H. Khan, M. Ali, *et al.*, Insight into microplastics in the aquatic ecosystem: Properties, sources, threats and mitigation strategies, *Sci. Total Environ.*, 2024, **913**, 169489.
3 C. G. Eze, C. E. Nwankwo, S. Dey, *et al.*, Food chain microplastics contamination and impact on human health: a review, *Environ. Chem. Lett.*, 2024, **22**(4), 1889–1927.
4 S. Goswami, S. Adhikary, S. Bhattacharya, *et al.*, The alarming link between environmental microplastics and health hazards with special emphasis on cancer, *Life Sci.*, 2024, **355**, 122937.
5 E. M. Kinyua, G. W. A. Nyakairu, E. Tebandeke, *et al.*, Photocatalytic Degradation of Microplastics: Parameters Affecting Degradation, *Adv. Environ. Eng. Res.*, 2023, **04**(03), 1–21.
6 L. L. Tian, Q. Q. Chen, W. Jiang, *et al.*, A carbon-14 radiotracer-based study on the phototransformation of polystyrene nanoplastics in water versus in air, *Environ. Sci.: Nano*, 2019, **6**(9), 2907–2917.
7 A. Bianco, F. Sordello, M. Ehn, *et al.*, Degradation of nanoplastics in the environment: Reactivity and impact on atmospheric and surface waters, *Sci. Total Environ.*, 2020, **742**, 140413.
8 J. H. Ge, Z. P. Zhang, Z. Z. Ouyang, *et al.*, Photocatalytic degradation of (micro)plastics using TiO_2-based and other catalysts: Properties, influencing factor, and mechanism, *Environ. Res.*, 2022, **209**, 112729.
9 Y. D. Luo, H. Zheng, X. Li, *et al.*, Modulating reactive oxygen species in O, S co-doped C_3N_4 to enhance photocatalytic degradation of microplastics, *Acta Phys.-Chim. Sin.*, 2025, **41**(6), 100052.
10 D. Jaimes, L. Patricia, C. González, *et al.*, Degradation of primary nanoplastics by photocatalysis using different anodized TiO_2 structures, *J. Hazard. Mater.*, 2021, **413**, 125452.
11 Á. E. R. Olivares, J. L. Guzmán-Mar, P. C. Quero-Jiménez, *et al.*, Analytical approaches to track nylon 6 microplastic fiber degradation using HKUST-1(Cu/Fe)-derived CuO/TiO_2 photocatalyst, *J. Water Process Eng.*, 2025, **71**, 107192.
12 M. Zheng, W. L. Xu, H. C. Yuan, *et al.*, Mesostructured perovskite solar cells based on Zn_2SnO_4 Single Crystal Mesoporous Layer with efficiency of 18.32%, *J. Alloys Compd.*, 2020, **823**, 153730.
13 S. D. Bertagna and A. C. Marques, TiO_2-based photocatalytic degradation of microplastics in water: Current status, challenges and future perspectives, *J. Water Process Eng.*, 2025, **72**, 153730.
14 P. Ebrahimbabaie, K. Yousefi and J. Pichtel, Photocatalytic and biological technologies for elimination of microplastics in water: Current status, *Sci. Total Environ.*, 2022, **806**, 150603.
15 C. R. Santos, G. P. Drumond, V. R. Moreira, *et al.*, Microplastics in surface water: occurrence, ecological

implications, quantification methods and remediation technologies, *Chem. Eng. J.*, 2023, **474**, 144936.
16 J. Jeyaraj, V. Baskaralingam, T. Stalin, *et al.*, Mechanistic vision on polypropylene microplastics degradation by solar radiation using TiO_2 nanoparticle as photocatalyst, *Environ. Res.*, 2023, **233**, 116366.
17 D. Aragón, C. Barquín, E. Bringas, *et al.*, Unravelling the photocatalytic degradation of polyethylene microplastics with TiO_2 under UV light: Evidence from kinetic studies, *Chem. Eng. J.*, 2025, **522**, 166672.
18 P. Chattopadhyay, M. C. A. Tarazona, E. I. C. González, *et al.*, Combining photocatalytic collection and degradation of microplastics using self-asymmetric Pac-Man TiO_2, *Nanoscale*, 2023, **15**(36), 14774–14781.
19 Y. L. He, A. U. Rehman, M. X. Xu, *et al.*, Photocatalytic degradation of different types of microplastics by TiOx/ZnO tetrapod photocatalysts, *Heliyon*, 2023, **9**(11), e22562.
20 Y. F. Zhu, H. C. Shen, Q. Ai, *et al.*, Double Layer SiO_2-Coated Water-Stable Halide Perovskite as a Promising Antimicrobial Photocatalyst under Visible Light, *Nano Lett.*, 2024, **24**(43), 13718–13726.
21 Y. F. Zhu and J. Zhang, Antimony-Based Halide Perovskite Nanoparticles as Lead-Free Photocatalysts for Controlled Radical Polymerization, *Macromol. Rapid Commun.*, 2024, **45**(9), 2300695.
22 L. Zhao, P. Zhang, L. J. Li, *et al.*, Revealing the potential of quantum dot nanomaterials in photocatalytic applications, *Chemosphere*, 2024, **361**, 142547.
23 C. Das, M. Sillanpää, S. A. Zaidi, *et al.*, Current trends in carbon-based quantum dots development from solid wastes and their applications, *Environ. Sci. Pollut. Res.*, 2023, **30**, 45528–45554.
24 B. Chon, S. Choi, Y. Seo, *et al.*, InP-Quantum Dot Surface-Modified TiO_2 Catalysts for Sustainable Photochemical Carbon Dioxide Reduction, *ACS Sustain. Chem. Eng.*, 2022, **10**(18), 6033–6044.
25 W. Gao, S. R. Zhang, G. Q. Wang, *et al.*, A review on mechanism, applications and influencing factors of carbon quantum dots based photocatalysis, *Ceram. Int.*, 2022, **48**(24), 35986–35999.
26 Q. Wang, T. Wang, N. Laila, *et al.*, Carbon dots/TiO_2 enhanced visible light-assisted photocatalytic of leachate: Simultaneous effects and Mechanism insights, *Water Res.*, 2023, **245**, 120659.
27 S. W. Xu, S. Zhang, H. G. Zhao, *et al.*, Electrostatic Attraction-Driven Interaction between TiO_2 and Colloidal Carbon Quantum Dots for Enhanced Visible Light Photocatalytic Degradation of Tetracycline and Antibacterial Activity Analysis, *Catal. Lett.*, 2025, **155**(3), 115.
28 R. J. P. Latiza, J. Olay, C. Eguico, *et al.*, Environmental applications of carbon dots: Addressing microplastics, air and water pollution, *J. Hazard. Mater. Adv.*, 2025, **17**, 100591.
29 H. Y. Qin, L. Sun, S. C. Zou, *et al.*, Boosted photocatalytic H_2O_2 production in pure water with amino-modified N, S-doped carbon dots, *Chem. Eng. J.*, 2024, **499**, 156239.
30 X. Yang, L. Ai, J. K. Yu, *et al.*, Photoluminescence mechanisms of red-emissive carbon dots derived from non-conjugated molecules, *Sci. Bull.*, 2022, **67**(14), 7.
31 Y. L. Cheng, M. S. Bai, J. Su, *et al.*, Synthesis of fluorescent carbon quantum dots from aqua mesophase pitch and their photocatalytic degradation activity of organic dyes, *J. Mater. Sci. Technol.*, 2019, **35**(8), 1515–1522.
32 P. Dukek, D. Schleheck and M. Kovermann, High-resolution NMR spectroscopic approaches to quantify PET microplastics pollution in environmental freshwater samples, *Chemosphere*, 2024, **367**, 143657.
33 Y. Y. Zhang, G. S. Yuan, X. K. Meng, *et al.*, Promoting the catalytic activities of polyanilines for l-lactic acid condensation by calcium-doping: A biocompatible strategy, *Chin. Chem. Lett.*, 2025, **36**(12), 111069.
34 M. Zheng, W. L. Xu, J. Xiao, *et al.*, Hierarchically Anatase TiO_2 microspheres composed of tiny octahedra used as mesoporous layer in perovskite solar cells, *Electrochim. Acta*, 2020, **331**, 135281.
35 M. Khalil, E. S. Anggraeni, T. A. Ivandini, *et al.*, Exposing TiO_2 (001) crystal facet in nano Au-TiO_2 heterostructures for enhanced photodegradation of methylene blue, *Appl. Surf. Sci.*, 2019, **487**, 1376–1384.
36 R. Katal, S. Masudy-Panah, M. Tanhae, *et al.*, A review on the synthesis of the various types of anatase TiO_2 facets and their applications for photocatalysis, *Chem. Eng. J.*, 2020, **384**, 123384.
37 R. M. S. Sendao, J. C. G. E. Silvaa, L. P. Silva, *et al.*, Photocatalytic removal of pharmaceutical water pollutants by TiO_2–Carbon dots nanocomposites: A review, *Chemosphere*, 2022, **301**, 134731.
38 Q. Wang, T. Wang, N. Laila, *et al.*, Carbon dots/TiO_2 enhanced visible light-assisted photocatalytic of leachate: Simultaneous effects and Mechanism insights, *Water Res.*, 2023, **245**, 120659.
39 B. Klahr and T. Hamann, Water Oxidation on Hematite Photoelectrodes: Insight into the Nature of Surface States through In Situ Spectroelectrochemistry, *J. Phys. Chem. C*, 2014, **118**, 10393–10399.
40 A. R. C. Bredar, A. L. Chown, A. R. Burton, *et al.*, Electrochemical Impedance Spectroscopy of Metal Oxide Electrodes for Energy Applications, *ACS Appl. Energy Mater.*, 2020, **3**(1), 66–98.
41 A. M. Torres-Huerta, D. Palma-Ramírez, M. A. Domínguez-Crespo, *et al.*, Comparative assessment of miscibility and degradability on PET/PLA and PET/chitosan blends, *Eur. Polym. J.*, 2014, **61**, 285–299.
42 G. Colomines, A. Lee, J. J. Robin, *et al.*, X-ray diffraction of the crystallinity of glycolysates derived from PET, *Eur. Polym. J.*, 2008, **44**, 2874–2885.
43 S. S. Zamir, B. Fathi, A. Ajji, *et al.*, Phase transition and crystallization behavior of grafted starch nanocrystals in PLA nanocomposites, *eXPRESS Polym. Lett.*, 2022, **16**(12), 1253–1266.
44 A. M. Torres-Huerta, D. Palma-Ramírez, M. A. Domínguez-Crespo, *et al.*, Comparative assessment of miscibility and

degradability on PET/PLA and PET/chitosan blends, *Eur. Polym. J.*, 2014, **61**, 285–299.

45 I. R. Macdonald, R. F. Howe, X. Y. Zhang, *et al.*, In situ EPR studies of electron trapping in a nanocrystalline rutile, *J. Photochem. Photobiol., A*, 2010, **216**(2–3), 238–243.

46 X. R. Xiao, Y. Chen, L. Feng, *et al.*, Selective Oxidation of Tertiary Alcohols to Ketones via Synergistic Catalysis of $(NH_4)_2Ce(NO_3)_6$ and Trifluoroacetic Acid With Oxygen, *cMat*, 2025, **2**, e35.

47 D. Zhou, H. Luo, F. Z. Zhang, *et al.*, Efficient Photocatalytic Degradation of the Persistent PET Fiber-based Microplastics over Pt Nanoparticles Decorated N-doped TiO_2 Nanoflowers, *Adv. Fiber Mater.*, 2022, **4**, 1094–1107.

48 M. C. A. Tarazon, C. Siligardi, H. A. Carreon-Lopez, *et al.*, The photodegradation processes and mechanisms of polyvinyl chloride and polyethylene terephthalate microplastic in aquatic environments: Important role of clay minerals, *Water Res.*, 2022, **208**, 117879.

49 E. O. Kruszkowska, I. Koter, J. S. Wiśniewska, *et al.*, Degradation of polylactide composites under UV irradiation at 254 nm, *J. Photochem. Photobiol., A*, 2015, **311**, 144–153.

50 X. Yang, R. Zhao, H. Zhan, *et al.*, Modified Titanium dioxide-based photocatalysts for water treatment: Mini review, *Environ. Funct. Mater.*, 2024, **3**(1), 1–12.